Broadband Radar Cross Section Reduction of Microstrip Antenna Using Polarization Conversion Metasurface

Krunal Patel[1, *] and Manjusha Joshi[2]

Abstract—Low Radar Cross Section antennas attract substantial attention in Stealth Technology. The Radar Cross Section reduction performance of the microstrip antennas should be improved since they contribute to the overall Radar Cross Section. A novel microstrip patch antenna with a Polarization Converter Metasurface (PCM) is proposed to extend the Radar Cross Section (RCS) reduction bandwidth. The metasurface uses metallic strip structures to obtain the required polarization conversion for Radar Cross Section reduction. The proposed patch antenna shows the overall RCS reduction bandwidth of 7.25 GHz–24.83 GHz (110%) as compared to the metal sheet and the Reference Patch antenna. 10 dB RCS reduction is obtained from 8.33 GHz–9.16 GHz (9.49%) and from 12.81 GHz–18.85 GHz (38.16%) as compared with the Reference Patch antenna. The RCS reduction of the antenna and the antenna radiation patterns are verified by numerical simulations and experimental observations. The main novelty of the proposed design is its wideband RCS reduction for Transverse Electric as well as Transverse Magnetic polarization with enhancement in antenna radiation pattern parameters. Significant RCS reduction can also be obtained for oblique incidence.

1. INTRODUCTION

Metasurfaces are used to manipulate the properties of the incident waves. Antennas are the key components on the combat platforms, and they are the greatest contributors to the total Radar Cross Section (RCS). So, it is desired that the antennas should be imperceptible. At the same time, the radiation pattern and other performance parameters of the antennas should not be degraded. Metasurfaces have the greatest capability of influencing the properties of electromagnetic waves. The most emerging applications of metasurfaces include the design of polarization converters, absorbers, and artificial magnetic conductors. With the developments in Radar Stealth Technology, new techniques of RCS reduction are being developed. A chessboard superstrate was suggested for RCS reduction of microstrip patch antenna in [1]. The structure showed RCS reduction for the frequency range of 8–14 GHz (54.5%). On the top side of the superstrate, a combination of two Artificial Magnetic Conductors (AMCs) was used. The bottom side of the superstrate structure consisted of a Fabri-Parot Resonant Cavity. The superstrate was located 16 mm away from the patch. So, the height of the antenna was increased. A polarization converter metasurface with a Micro-Electromechanical System (MEMS) switch was designed in [2]. The metasurface converted linear polarization into its orthogonal polarization over the frequency range of 7.93 GHz–12.42 GHz (44.13%) when the switch was ON. It converted the linearly polarized wave into a circularly polarized wave from 8.07 GHz–10.77 GHz (28.66%). The design was complex due to the inclusion of the MEMS switch. It was not utilized for RCS reduction. In [3], a triangle type checkerboard surface was reported to reduce the RCS of a planar surface. The −8 dB RCS reduction bandwidth was from 59 GHz to 73 GHz (21.2%). The structure showed less angular stability after 45 deg angle of incidence. It was not utilized to reduce the RCS of a patch antenna.

A coding diffuse metasurface was proposed in [4] which was based on ergodic algorithm optimization. The metasurface provided the 10 dB RCS reduction bandwidth from 5.4 GHz to 7.4 GHz (31.25%). An L-shaped polarization converter metasurface was discussed in [5] which offered polarization conversion ratio greater than 90% over the frequency range of 8.6 GHz–22 GHz (FBW 88%). The metasurface was designed on an F4B substrate. The metasurface was not used for RCS reduction of a patch antenna. Characteristic Mode Analysis of the linear to circular polarization converter metasurface was presented in [6]. Liu et al. [7] designed a microstrip patch antenna with a polarization conversion metasurface. The overall RCS reduction was observed for the frequency range of 3–12 GHz (120%). For this antenna, −10 dB RCS reduction bandwidth was not discussed, and it showed narrowband performance for the same. The gain values for the reference patch and the low-RCS antenna were not compared. The design exhibited good radiation pattern characteristics. In [8], a pixelated checkerboard metasurface was used to achieve RCS reduction over the frequency range of 3.8–10.7 GHz (95.17%). A binary optimization algorithm was presented in this literature, but the design was not studied for RCS reduction of a patch antenna. Zhang et al. [9] developed an AMC based metasurface with the help of a circular ring structure with a parasitic cross within it. The dimensions of the unit cells were varied to obtain the required phase difference. But the RCS reduction was observed from 8.2–10.25 GHz (22.22%) which exhibited narrowband performance. Detailed analysis of metamaterial absorbers was presented in [10] which showed that absorbers exhibited strong resonant properties. Because of this reason their performance is band-limited in nature. Absorption greater than 80% was reported for a symmetric absorber from the frequency range of 3.08–3.13 GHz (1.61%) which showed narrowband performance. Traditional methods of using radar absorbing materials [11] degrade the antenna radiation pattern. It is evident from the literature review that most of the metasurfaces are not used for RCS reduction of patch antennas [14]. If radar absorbing materials are used, then they degrade the antenna radiation pattern. Metamaterial absorbers [19, 20] are band limited in nature, and target shaping methods are not suitable for the aerodynamic shape of the weapon. So, it is desired to explore such a design that can provide wide RCS reduction bandwidth without degradation in antenna radiation pattern. RCS reduction should be obtained for normal as well as oblique incidence. In this paper, a novel polarization conversion metasurface is proposed, and it is integrated with the patch antenna. The RCS reduction performance of the designed antenna is analyzed for transverse electric (TE) as well as transverse magnetic (TM) modes. With this novel design, the RCS of the patch antenna can be reduced significantly with an enhancement in radiation pattern characteristics. Wideband RCS reduction can be achieved for parallel as well as perpendicular polarization.

2. DESIGN OF THE UNIT CELL AND THE POLARIZATION CONVERTER METASURFACE

A metallic strip structure is used to design the unit cell of the metasurface as shown in Fig. 1. The unit cell has advantages in terms of its geometry, resonant frequency control, and polarization conversion characteristics. The length and width of the metallic strip are $ls = 6.8$ mm and $ws = 1.5$ mm, respectively. An FR-4 substrate with the dielectric constant $\varepsilon_r = 4.3$ is chosen to design the metasurface unit cell. The height of the substrate is $h = 4.3$ mm. The substrate is backed by a metallic ground of copper. The thickness of Cu is 0.035 mm. The metallic strip structure is rotated by an angle of 45 deg to design a polarization converter metasurface. The parametric analysis is done in CST Microwave Studio software to arrive at the optimum dimensions of the metasurface unit cell. The resonant frequencies can be changed by changing the width and length of the metallic strip.

Figure 2 shows the co-polarized reflection coefficient and cross-polarized reflection coefficient of the metasurface unit cell for the TE mode. It shows three plasmonic resonances at 9.1037 GHz, 13.655 GHz, and 20.498 GHz. At these frequencies, the co-polarized reflection coefficient is minimized, and the cross-polarized reflection coefficient is maximized. The values of polarization conversion ratios [16] are near unity at these frequencies. The mechanism of the polarization conversion can be explained with the help of S-parameters and surface current theory. Fig. 3 shows the co-polarized reflection coefficient and cross-polarized reflection coefficient of the metasurface unit cell for the TM mode. The reflection coefficients are almost similar due to the structural symmetry of the unit cell.

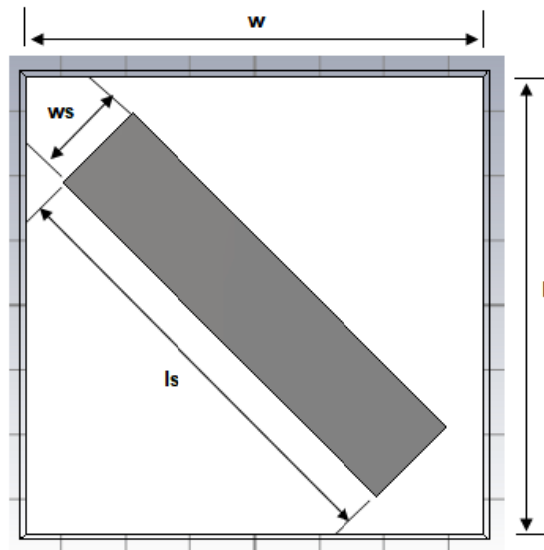Figure 4(a) shows that the incident wave is decomposed into two orthogonal components. One

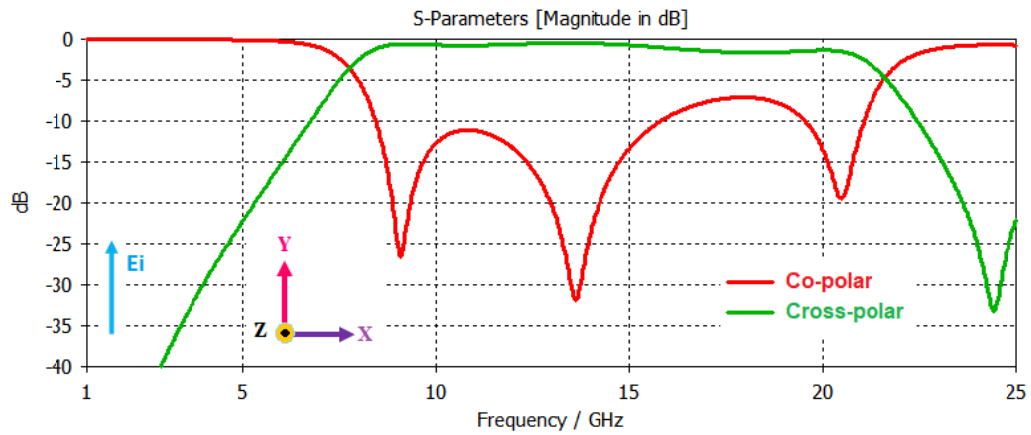**Figure 1.** Design of the unit cell of the metasurface.

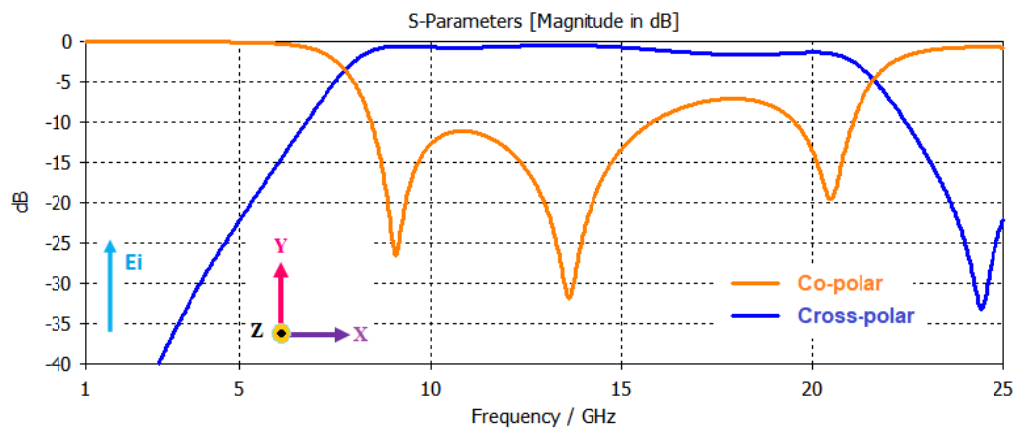**Figure 2.** Co-polarized and cross-polarized reflection coefficients for TE mode.

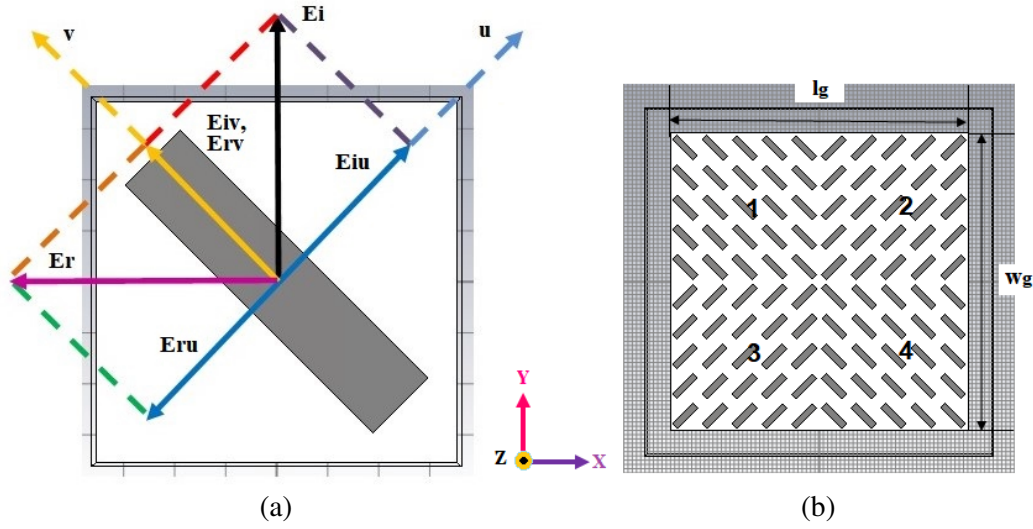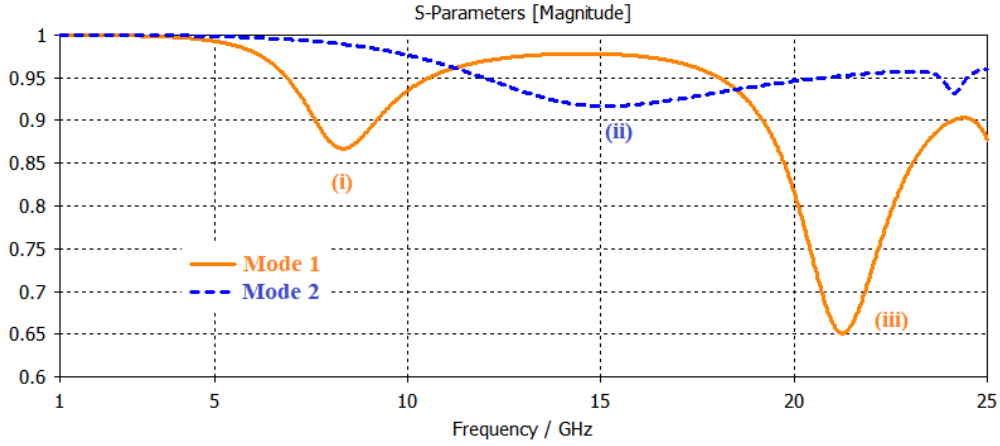**Figure 3.** Co-polarized and cross-polarized reflection coefficients for TM mode.

(a)   (b)

Figure 4. (a) Mechanism of polarization conversion. (b) Design of the polarization converter metasurface.

Figure 5. Reflection coefficients of u-polarized and v-polarized waves.

component is u-polarized wave, and the other is v-polarized wave. It also shows the mechanism of polarization conversion. E_i is the incident electric field, and E_r is the reflected electric field. A detailed description on this mechanism is included in the subsequent discussions. To design the polarization converter metasurface, all the unit cells are arranged in the mirror configuration as shown in Fig. 4(b). To explain the general mechanism of RCS reduction, the metasurface is divided into four regions. If the reflected fields from Region 1 are in the $-x$-direction, then the reflected fields from adjacent Region 2 will be in the $+x$ direction. So, whenever a wave is incident on the metasurface, the reflected fields from adjacent regions are cancelled, and the echo signal cannot reach the radar receiver resulting in excellent RCS reduction. If all the unit cells are arranged in the same direction, then no RCS reduction can be observed.

As shown in Fig. 5, eigen-modes (i) and (iii) are due to the v-polarized wave, and eigen-mode (ii) is due to the u-polarized wave. Mode 1 is considered as the v-polarized wave, and Mode 2 is considered as the u-polarized wave. So, overall three plasmonic resonances can be observed over the frequency range of 5 GHz–25 GHz. Fig. 6 shows the reflection phases of the u-polarized wave and v-polarized wave.
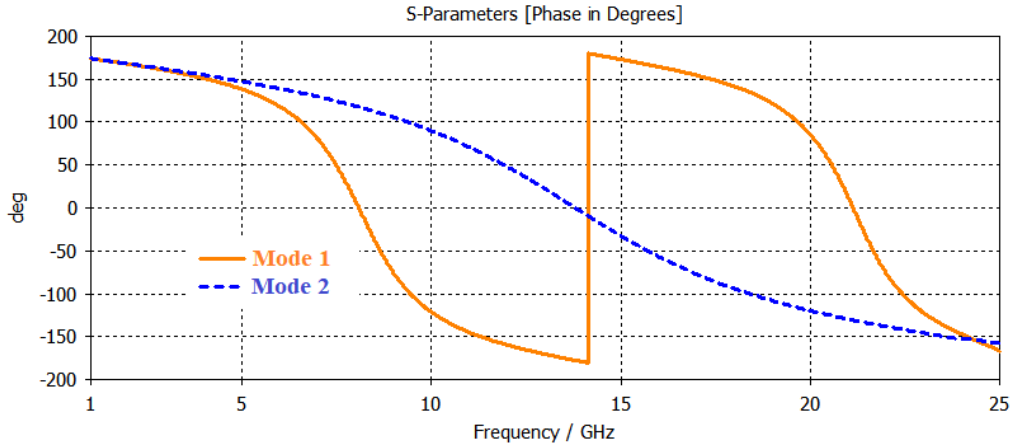
Figure 6. Reflection phase of u-polarized and v-polarized waves.

The reflected electric field can be obtained by [21]

$$\vec{E} = -i\frac{\omega\mu}{4\pi} \int \vec{J}(x,y) \frac{e^{-ikR}}{R} \, dxdy \tag{1}$$

where E = Electric field intensity; J = Electric surface current density; R = distance between the observation point and the source; μ is the permittivity of the material; k is the free-space wave number; and ω is the angular frequency. For calculating the electric field, the integration should be calculated over the surface of the metasurface.

The co-polarized reflection coefficient can be expressed as [17],

$$\Gamma_{yy} = \frac{E_{ry}}{E_{iy}} = \sqrt{\frac{(1 + \cos\Delta\phi)}{2}} \tag{2}$$

The cross-polarized reflection coefficient is written as [17],

$$\Gamma_{xy} = \frac{E_{rx}}{E_{iy}} = \sqrt{\frac{(1 - \cos\Delta\phi)}{2}} \tag{3}$$

where E_r = magnitude of the reflected electric field, E_i = magnitude of the incident Electric field, and $\Delta\phi$ = reflection phase difference between the u and v-components.

So, whenever the value of $\Delta\phi$ is $\pm 180°$, the values of co-polarized reflection coefficient and cross-polarized reflection coefficients are 0 and 1, respectively.

As shown in Fig. 7, the resonant frequencies of the unit cell can be controlled by changing the width and height of the unit cell. If the width of the strip is increased, then the resonant frequencies of the first two resonances decrease, and the resonant frequencies of the third resonance increase. There is no significant effect on the cross-polar performance if the width of the strip is changed. If the length of the strip is increased, then the resonant frequencies of the first resonance can be controlled, and the resonant frequency of the second resonance is slightly affected as shown in Fig. 8. The resonant frequency of the third resonance remains almost the same for different values of the length. The cross-polar reflection remains almost unaffected by the changes in the values of the length.

Figure 9 shows the surface current distribution of the metallic strip on the top side and the ground plane on the bottom side of the metasurface unit cell. The black arrow indicates the direction of the surface current. If the directions of the surface current on the top side and on the ground plane are the same, then the structure behaves like a perfect electric conductor, and the reflected field is out of phase by 180 deg with respect to the incident field. It exhibits electric resonance. If the directions of the surface currents on the top side and bottom side are opposite, then it shows the magnetic resonance. As per Maxwell's equation, the time-varying magnetic field will result in the curling electric field resulting in magnetic resonance. The reflected field will be in-phase with respect to the incident field, and
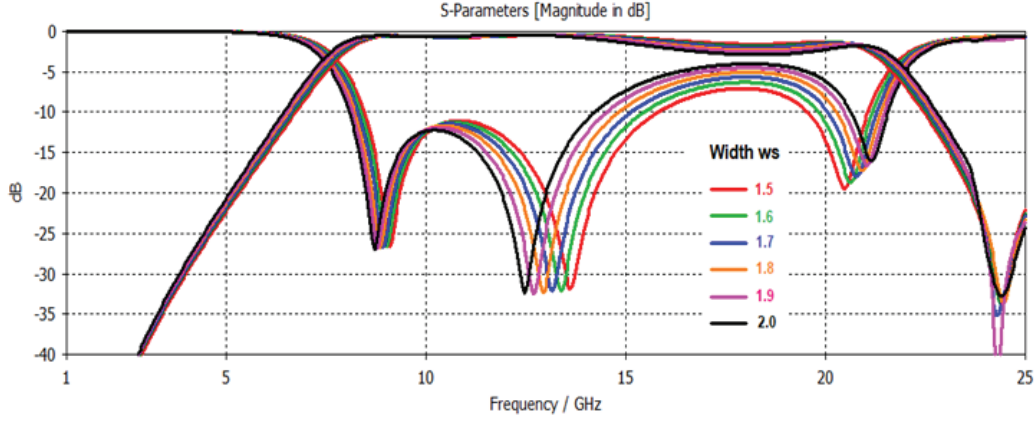
Figure 7. Resonant frequency control by changing the width of the strip.
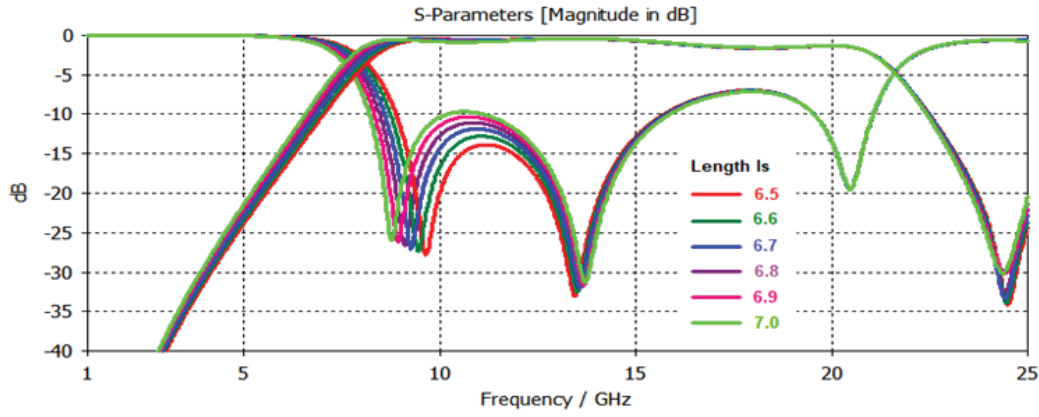
Figure 8. Resonant frequency control by changing the length of the strip.

the structure shows Artificial Magnetic Conductor (AMC) behaviour. At a particular frequency, one component of the incident field shows the electric resonance, and the orthogonal component shows the magnetic resonance. So, either the u-polarized or v-polarized wave undergoes 180 deg phase shift, and the orthogonal component undergoes 0 deg phase shift. So the resultant field vector will be in the direction of E_r, and the cross-polar reflection will be maximized. As shown in Fig. 9(a) and Fig. 9(c), magnetic resonance can be observed for the v-polarized wave at the resonant frequencies of 9.1037 GHz, and electric resonance is observed at the frequency of 20.498 GHz for the same. As shown in Fig. 9(b), magnetic resonance can be observed for the u-polarized wave at the resonant frequency of 13.655 GHz. If the vector addition of the reflected field components is taken, then the resultant vector will be in the orthogonal direction indicating cross-polarization conversion.

The AMC behaviour for a particular component can also be explained with the help of the reflection coefficient. The reflection coefficient $\Gamma(\omega)$ at normal incidence is given by,

$$\Gamma(\omega) = \frac{\eta(\omega) - \eta_0}{\eta(\omega) + \eta_0} \tag{4}$$

where $\eta(\omega)$ is the impedance which varies with frequency, and η_0 is the free-space impedance. If $\eta(\omega) \gg \eta_0$, then the magnitude of the reflection coefficient is nearly one, and its phase is 0 deg. So, the metasurface has high impedance, and it behaves like an artificial magnetic conductor. If the magnetic flux in the dielectric medium is strengthened because of the oppositely directed currents, then the effective magnetic permeability increases, and it leads to higher surface impedance $\sqrt{(\mu/\varepsilon)}$. This High Impedance Surface (HIS) structure reflects the wave with 0 deg phase shift.
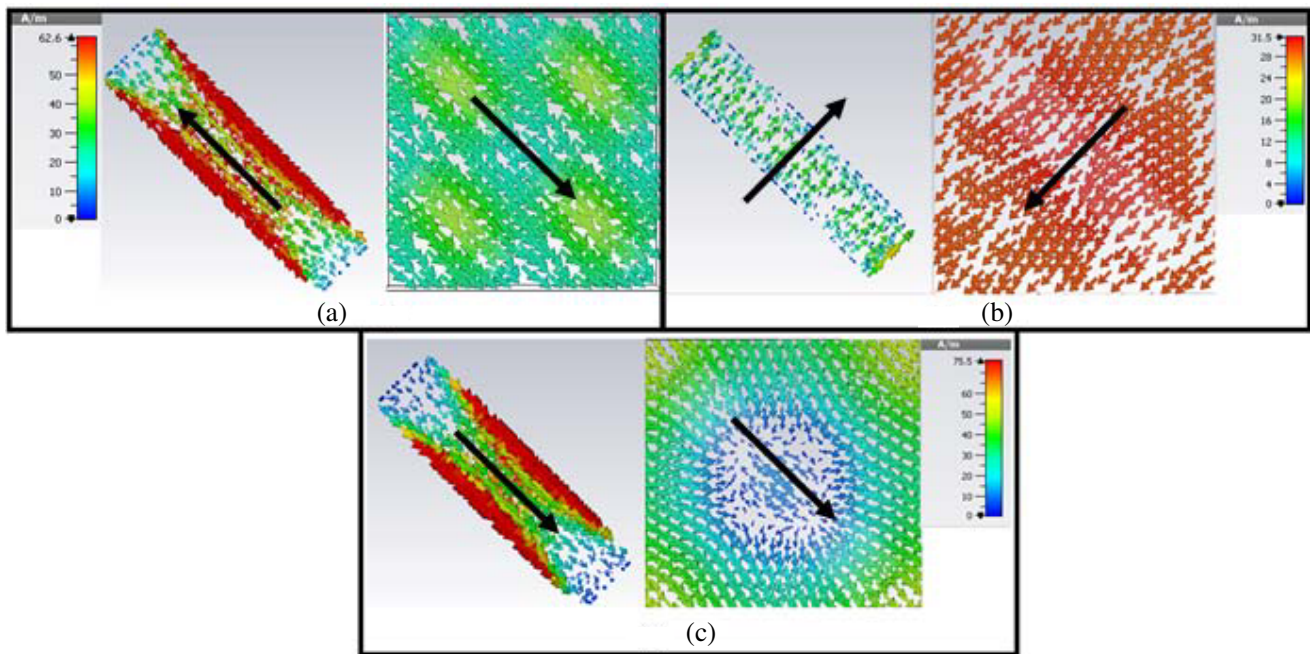
Figure 9. Surface current distribution at (a) 9.1037 GHz, (b) 13.655 GHz and (c) 20.498 GHz.
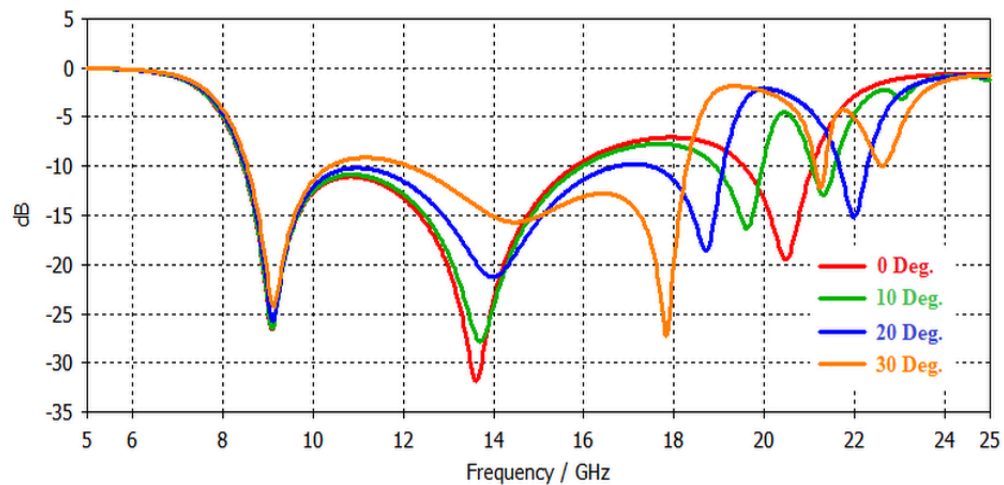

Figure 10. Co-polar reflection at oblique incidences (TE mode).

Figures 10 and 11 show the co-polar and cross-polar reflection coefficients respectively under oblique incidences up to 30 deg for the transverse electric mode. These figures show that the unit cell shows good polarization conversion under oblique incidences. In the case of co-polar reflection, the first resonant frequency remains almost the same for various angles of incidence, but the second and third resonances show frequency shift. The cross-polar reflection coefficient remains almost similar from 5 GHz to 18 GHz for oblique incidences. After that some variations are observed in it. However, good co-polar reflection reduction and cross-polar conversion ensure RCS reduction at oblique incidences.

Figures 12 and 13 show the co-polar and cross-polar reflection coefficients respectively under oblique incidences for the transverse magnetic mode. The resonant frequencies are similar to those of the TE mode. Slight changes in the magnitude of the reflection coefficient can be observed. The cross-polar reflection is almost similar to that of the TE mode.
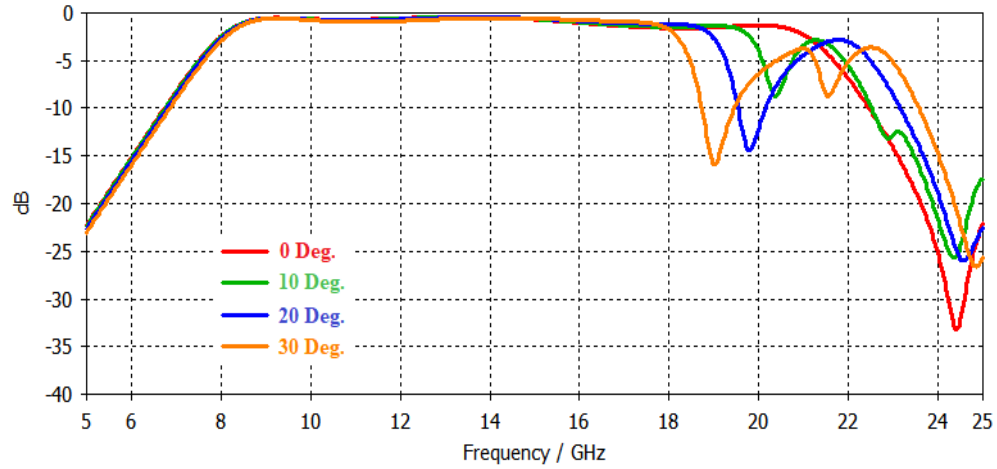
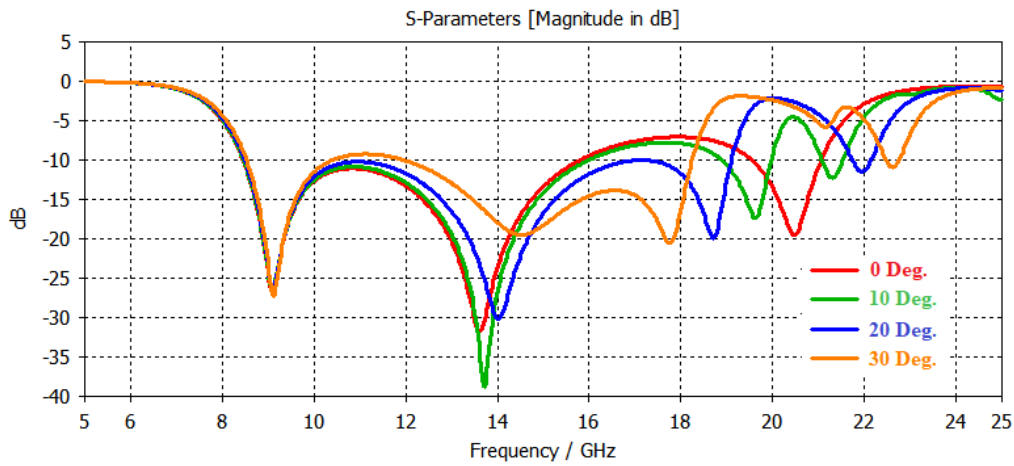**Figure 11.** Cross-polar reflection at oblique incidences (TE mode).

Figure 12. Co-polar reflection at oblique incidences (TM mode).
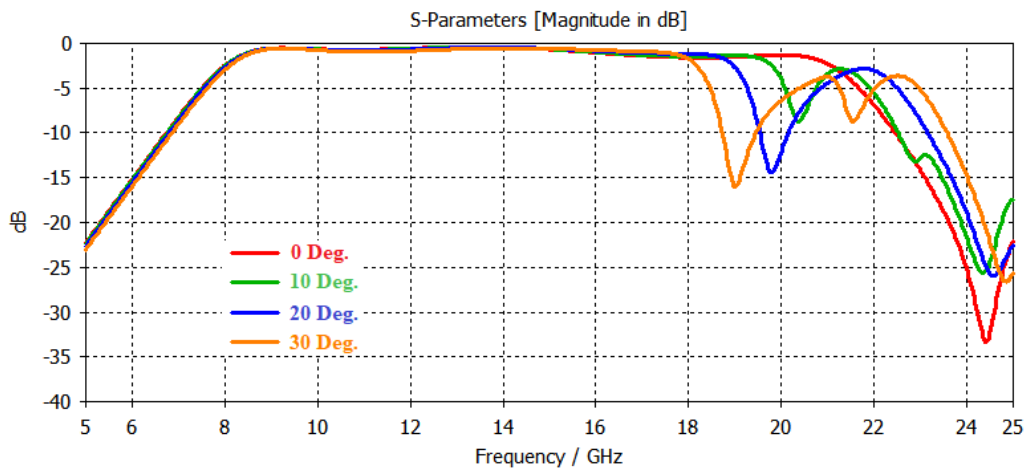

Figure 13. Cross-polar reflection at oblique incidences (TM mode).

The total scattering field from the metasurface can be found by the following array factor theory. For the array of A rows and B columns, the array factor is given by [21],

$$\text{AF} = \sum_{a=1}^{A} \sum_{b=1}^{B} e^{j\left[\left(a-\frac{1}{2}\right)(kd\sin\theta\cos\emptyset)+\left(b-\frac{1}{2}\right)(kd\sin\theta\sin\emptyset)+\delta(a,b)\right]} \tag{5}$$

where θ represents the angle between the plane wave and z-axis in the XZ plane, and ϕ is the angle between the plane wave and x-axis in the XY plane. The rows and columns are indicated by a and b, respectively. Symbol k is the free-space wave number; d represents the distance between the adjacent units; and $\delta(a,b)$ shows the phase difference between the array elements.

The proposed metasurface can be represented by the 01/10 coding scheme, and the reflected fields from the metasurface can be evaluated by the array factor theory.

The scattered field is given by,

$$E_{\text{total}} = \text{Field Pattern} \times \text{Array Factor} \tag{6}$$

The total scattered field is given by,

$$E_{\text{total}} = \text{FP}_0\text{AF}_0 + \text{FP}_1\text{AF}_1 \tag{7}$$

where FP_0 and FP_1 indicate the total reflected field patterns of the unit cell which is represented by '0' and the field pattern of the mirror cell which is represented by '1', respectively. For a 2×2 configuration, the array factor is given by,

$$\begin{aligned}\text{AF}_{2\times2} &= e^{j\left[\frac{1}{2}kd\sin\theta\cos\emptyset+\frac{1}{2}kd\sin\theta\sin\emptyset+\delta(1,1)\right]} + e^{j\left[\frac{3}{2}kd\sin\theta\cos\emptyset+\frac{3}{2}kd\sin\theta\sin\emptyset+\delta(2,2)\right]}\\&\quad + e^{j\left[\frac{1}{2}kd\sin\theta\cos\emptyset+\frac{3}{2}kd\sin\theta\sin\emptyset+\delta(1,2)\right]} + e^{j\left[\frac{3}{2}kd\sin\theta\cos\emptyset+\frac{1}{2}kd\sin\theta\sin\emptyset+\delta(2,1)\right]}\end{aligned} \tag{8}$$

In the above equation, $\delta(1,1)$ and $\delta(2,2)$ indicate 0 deg phase difference if the unit cells are arranged in the mirror configuration, and $\delta(1,2)$ and $\delta(2,1)$ indicate the phase difference of 180 deg for the adjacent cells of column and row, respectively. $\delta(1,2)$ can be represented by $2kd\sin\theta\sin\phi$ whereas $\delta(2,1)$ can be represented by $2kd\sin\theta\cos\phi$. Further simplification shows that,

$$\begin{aligned}\text{AF}_{2\times2} &= e^{j\frac{kd}{2}[\sin\theta\cos\emptyset+\sin\theta\sin\emptyset]} + e^{-j\frac{kd}{2}[\sin\theta\cos\emptyset+\sin\theta\sin\emptyset]}\\&\quad + e^{j\frac{kd}{2}[\sin\theta\sin\emptyset-\sin\theta\cos\emptyset]} + e^{-j\frac{kd}{2}[\sin\theta\sin\emptyset-\sin\theta\cos\emptyset]}\end{aligned} \tag{9}$$

The first two terms of the above equation correspond to AF_0, and the last two terms correspond to AF_1. For the normally incident wave, $\theta = 0$ and $\emptyset = 0$, and the value of AF_0 and AF_1 is 1/2 assuming that the area of the unit cell is 1. If E_i is the normally incident Electric field, then

$$\text{FP}_0 = \Gamma_{x_0x_0}E_i + \Gamma_{y_0x_0}E_i \tag{10}$$

$$\text{FP}_1 = \Gamma_{x_1x_1}E_i + \Gamma_{y_1x_1}E_i \tag{11}$$

where Γ_{xx} is the co-polarized reflection coefficient, and Γ_{yx} is the cross-polarized reflection coefficient. For the cells arranged in the '01/10' pattern, the reflection phases of the co-polar components are the same, but the cross-polar components are 180 deg out of phase. From Equation (7), the total scattered field is given by,

$$E_{\text{total}} = \left(\frac{1}{2}\right)\left[\Gamma_{x_0x_0}E_i + \Gamma_{x_1x_1}E_i + \Gamma_{y_0x_0}E_i + \Gamma_{y_1x_1}E_i\right] \tag{12}$$

$$E_{\text{total}} = \left(\frac{1}{2}\right)\left[\Gamma_{x_0x_0}E_i + \Gamma_{x_1x_1}E_i\right] = \Gamma_{xx}E_i \tag{13}$$

So, if the magnitude of the co-polar reflection coefficient decreases, then the co-polar reflected field is minimized. From the above equation, it can be inferred that the theoretical value of the co-polar reflection coefficient should be less than or equal to 0.31 for 10 dB RCS reduction.

3. ANTENNA DESIGN

For the selection of the metasurface, two designs were investigated. Design 1 resembles the 00/00 or 11/11 coding scheme, and Design 2 resembles the 01/10 coding scheme as shown in Fig. 14(a) and Fig. 14(b), respectively. The RCS reduction performance of the 00/00 or 11/11 coding scheme is compared with that of the 01/10 coding scheme. As shown in Fig. 15, the 00/00 or 11/11 coding scheme does not show RCS reduction since the unit cells are arranged in the same direction. The 01/10 coding scheme shows significant RCS reduction because of opposite phase cancellations from the adjacent regions. The metasurface is designed by turning the metallic strip structure by 45 deg. If other angles of rotation are used, then the structure loses the symmetry, and the response of the structure will be different for the Transverse Electric mode and the transverse magnetic mode even at the normal incidence. In this case, the required polarization conversion is not obtained. Design 2 shows significant RCS reduction over a wide bandwidth. So, the antenna is designed using the 01/10 coding scheme.


(a)   (b)
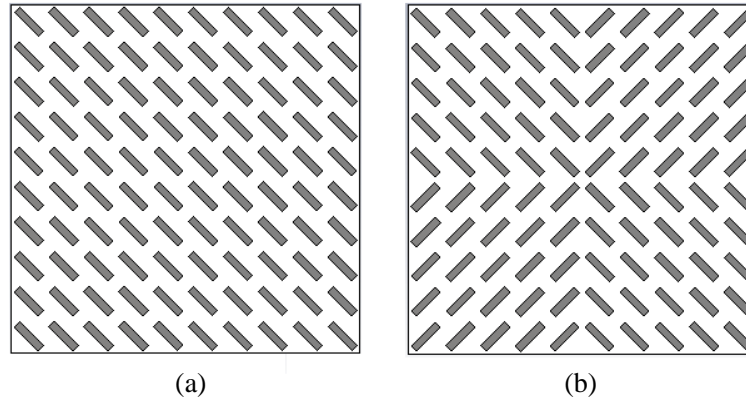
Figure 14. (a) Metasurface Design 1. (b) Metasurface Design 2.
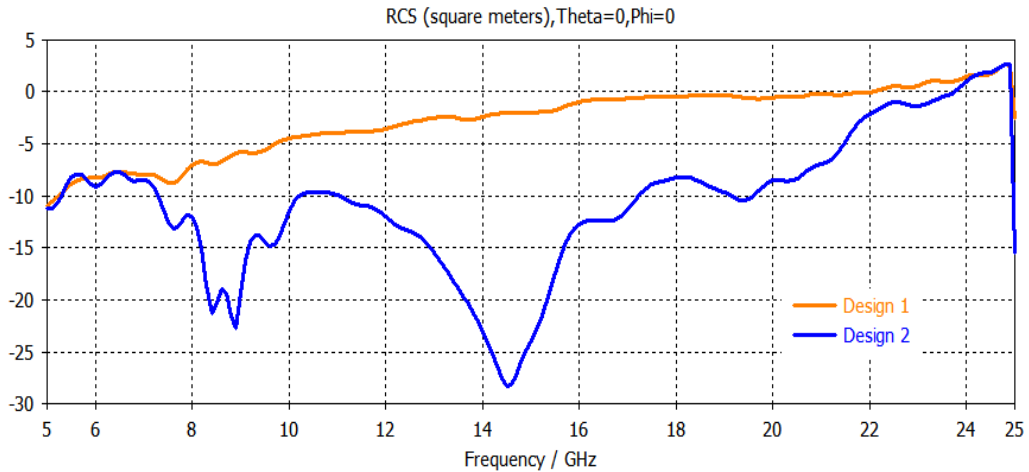

Figure 15. RCS comparison of Design 1 and Design 2.

To design a low RCS microstrip patch antenna, co-planar integration of the metasurface with the patch antenna is carried out. The antenna is considered perfectly matched with the feed line impedance facilitating the observation of the structural mode RCS of the antenna. Fig. 16 shows the geometry of the microstrip patch antenna with polarization converter metasurface. The low-RCS antenna is designed on the same FR-4 substrate having thickness (h) of 2.4 mm, dielectric constant (ε_r) of 4.3,
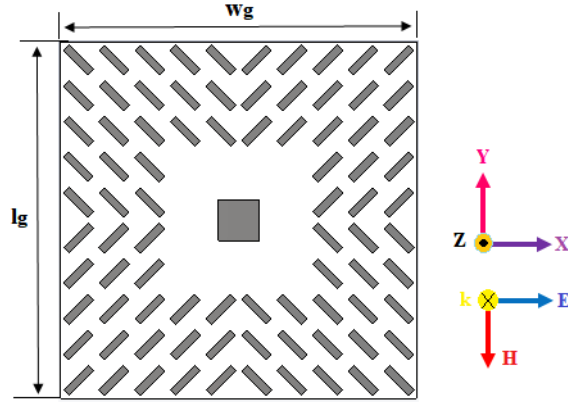
Figure 16. Microstrip patch antenna with polarization converter metasurface.

(a)   (b)   (c)   (d)
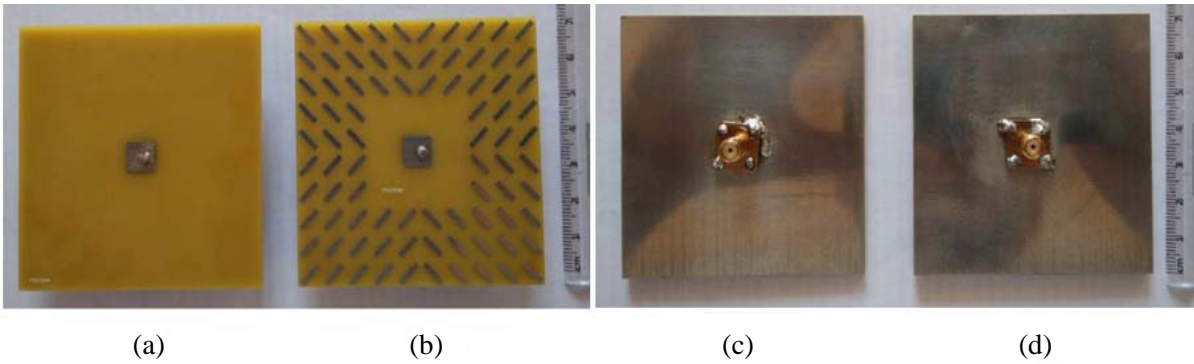
Figure 17. Top view of fabricated antennas, (a) Ref. Patch, (b) antenna with PCM; Bottom view of fabricated antennas, (c) Ref. Patch, (d) antenna with PCM.

and loss-tangent ($\tan \delta$) of 0.02. The square patch antenna has dimensions of $8 \, \text{mm} \times 8 \, \text{mm}$. The length and width of the ground plane and substrate are $l_g = 70 \, \text{mm}$ and $w_g = 70 \, \text{mm}$, respectively. The Cu thickness is $0.035 \, \text{mm}$. The low RCS antenna uses an array of 10×10 unit cells for coplanar integration with the patch antenna. An array of 4×4 unit cells was removed from the centre to facilitate microstrip patch antenna design. The dimensions of the array are chosen in such a way that adequate RCS reduction is obtained without degradation of the antenna radiation pattern. If more unit cells are removed, then the RCS reduction may not be sufficient. If fewer cells are removed, then the antenna radiation pattern may be degraded because of mutual coupling between the antenna and metasurface unit cells. If equal numbers of unit cells are not removed from the rows and columns, then the structure loses its symmetry. Fig. 17 shows the top and bottom views of the fabricated microstrip patch antennas. The patch antennas are fabricated on an FR-4 substrate with height $h = 2.4 \, \text{mm}$, dielectric constant $\varepsilon_r = 4.3$, and loss tangent $\tan \delta = 0.02$. They are fabricated using the standard Printed Circuit Board (PCB) fabrication technology.

The spacing between the patch antenna and the metasurface unit cell is chosen in such a way that the radiation pattern of the antenna does not degrade, and it does not show a tilted beam. The RCS reduction characteristics of the antenna are determined as follows.

The total RCS of a loaded antenna is given by,

$$\sigma = \left| \sqrt{\sigma^s} - (1 + \Gamma_A) \sqrt{\sigma^a} e^{j\phi_r} \right|^2 \qquad (14)$$

where σ = total RCS when the antenna is terminated with load impedance, σ^s = structural RCS, σ^a = antenna mode RCS, Γ_A = antenna reflection coefficient, ϕ_r = relative phase between σ^s and σ^a.

For an open circuited antenna reflection coefficient $\Gamma_A = 1$, and RCS in this mode is given by,

$$\sigma_{\text{open}} = \left| \sqrt{\sigma^s} - 2\sqrt{\sigma^a} e^{j\emptyset_r} \right|^2 \qquad (15)$$

For a matched antenna, RCS is given by,

$$\sigma_{\text{match}} = \left| \sqrt{\sigma^s} - \sqrt{\sigma^a} e^{j\emptyset_r} \right|^2 \qquad (16)$$

4. RESULTS AND DISCUSSION

The reference antenna and the low RCS antenna are simulated in CST Microwave Studio software. Fig. 18 shows the simulated RCS of the metal plate, the reference antenna, and the antenna with PCM.
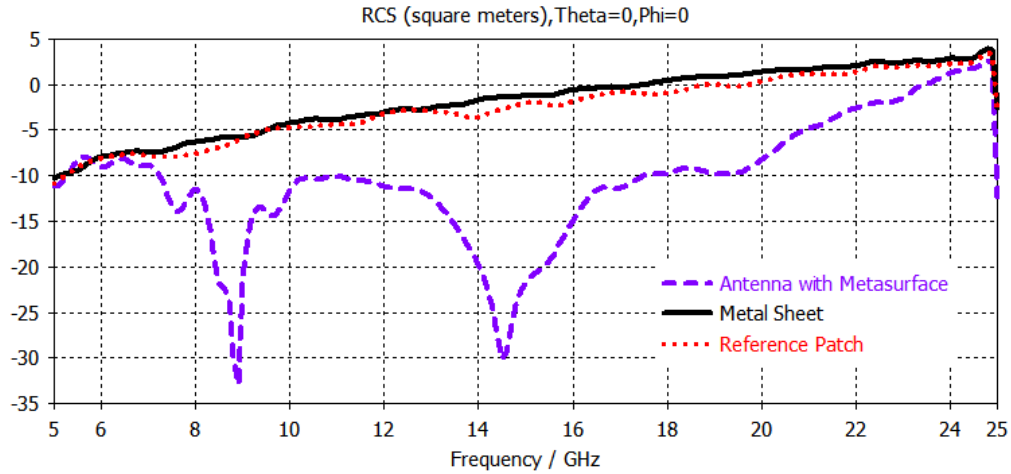

Figure 18. Simulated values of RCS (TE, TM modes).

From simulation results, it is observed that the overall RCS reduction bandwidth of 7.25 GHz–24.83 (110%) GHz is obtained as compared with the metal sheet and the reference patch antenna. 10 dB RCS reduction is obtained from 8.33 GHz–9.16 GHz (9.49%) and from 12.81 GHz–18.85 GHz (38.16%) as compared with the reference patch antenna. The RCS reduction peaks are observed at 8.9 GHz in the X-band and at 14.52 GHz in the Ku-band. The RCS values are -32.17 dBsm and -29.91 dBsm at these frequencies, respectively.
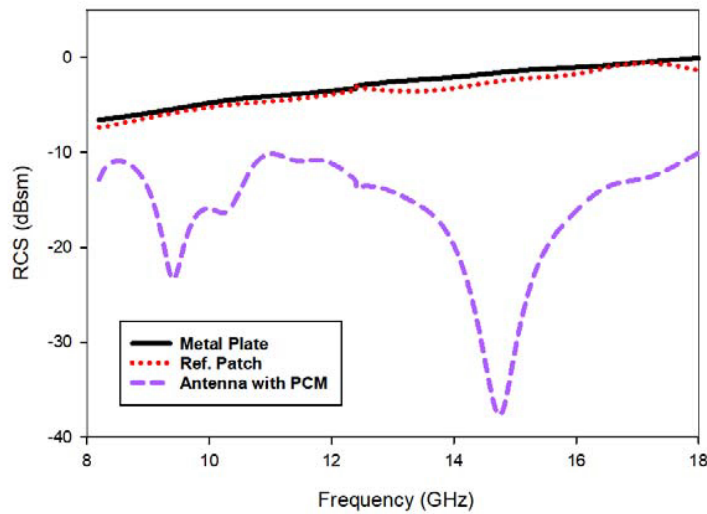
Experimental measurements of RCS were carried out in an anechoic chamber with 10 inch absorbers. Fig. 19 shows the experimental setup to measure the RCS values of the metal plate, the reference patch, and the antenna with PCM. Fig. 19(a) shows the transmitter-receiver horn antennas assembly. Fig. 19(b) shows the antenna mounted on the target positioning system.

Initially the target is placed within the Alias-Free-Range. A sphere of radius 15.24 cm is taken as a reference since its RCS values are independent of frequency. The samples are mounted on a thermocol stand, and they are aligned in the azimuthal and elevation directions through the positioning system. Then data acquisition is carried out with the help of control software for the reference patch, the antenna with PCM, and the metal plate of the same dimensions. The data is converted into the distance domain, and time gating is placed at an appropriate range. The gated data is used to calculate RCS of the samples in dBsm. Initially, the RCS of the same size of metal plate was obtained. Then the same procedure was repeated for the reference patch and the antenna with PCM.

Figure 20 shows the experimentally measured RCS values of the metal plate, the reference patch, and the antenna with PCM for the TE mode. The results show that the antenna with PCM shows an RCS reduction peak at 9.41 GHz in X-band, and the measured RCS value is -23.34 dBsm at this frequency. The design shows another RCS reduction peak at 14.745 GHz in Ku-band, and the measured RCS value is -37.66 dBsm. Because of the limitations of the experimental measurement setup, the

<div align="center">(a)   (b)</div>
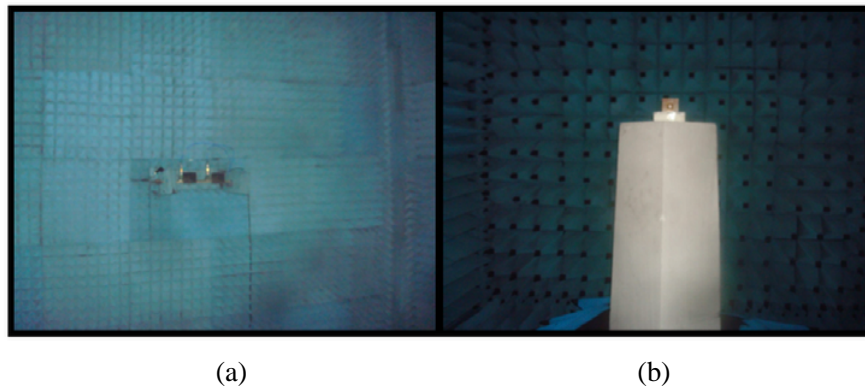
Figure 19. Experimental setup to measure RCS of the antennas. (a) Transmitter-receiver horn antennas. (b) Target positioning system.

Figure 20. Experimentally measured values of RCS (TE mode).

RCS measurements were carried out from 8–18 GHz. So, the structure shows good RCS reduction from 8–18 GHz. 10 dB RCS reduction bandwidths of 13.3% and 35.38% are obtained in the X-band and Ku-band, respectively. The simulated and experimentally measured results are in good agreement. Slight variations may be observed due to fabrication tolerances and limitations in the experimental measurement setup. Fig. 21 shows the experimentally measured RCS values for the samples in TM mode. Due to the structural symmetry of the design, the RCS results of the TM mode are almost similar to those of the TE mode for the normal incidence.

Figure 22 shows the RCS characteristics of the antenna with PCM under oblique incidences for the TE mode. Fig. 23 shows the RCS characteristics of the antenna with PCM under oblique incidences for the TM mode. It is inferred from the figures that the antenna shows good RCS reduction for angles of incidence up to 30 deg. If the angle of incidence is increased, then RCS reduction is also observed with some shifts in peak RCS reduction frequencies. These observations can also be verified by the values of reflection coefficients under oblique incidences.

Figure 24(a) shows the simulated reflection coefficients of the reference antenna and the antenna with PCM structures. Fig. 24(b) shows the experimentally measured reflection coefficient of the antenna with PCM.

The resonant frequency of the simple patch antenna is 7.53coefficient is around -17.5 dB. The simulated reflection coefficient of the antenna with PCM is around -17 dB at the resonant frequency
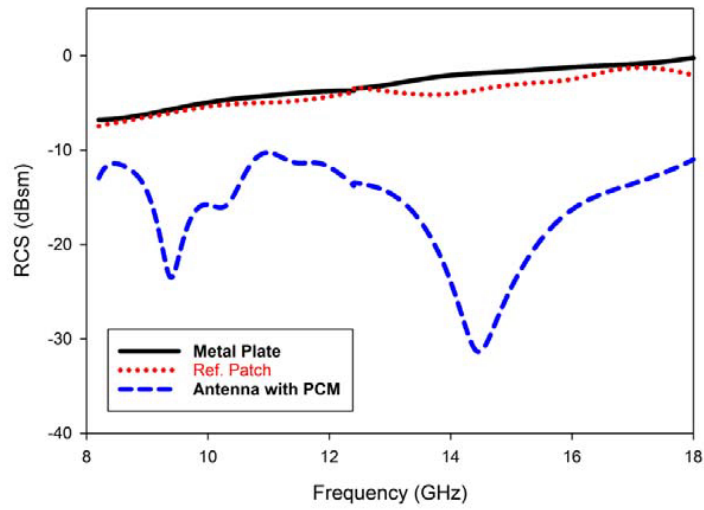
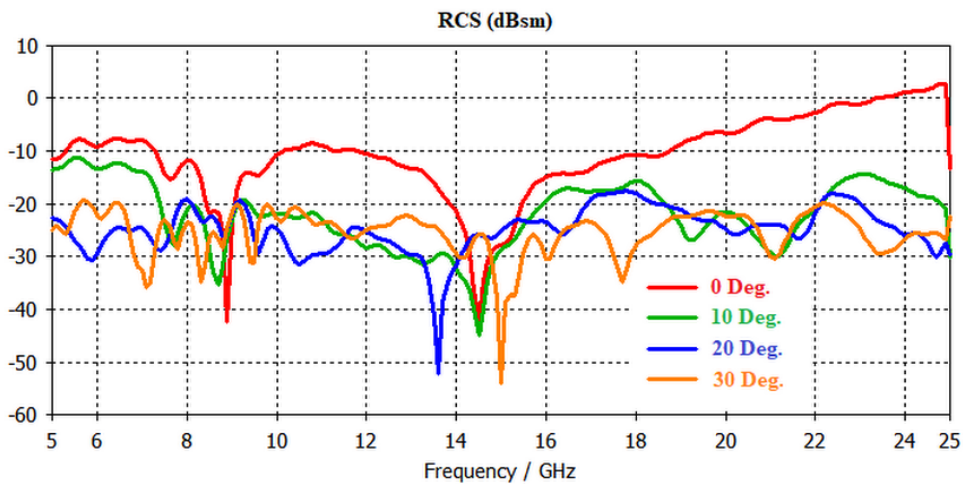**Figure 21.** Experimentally measured values of RCS (TM mode).

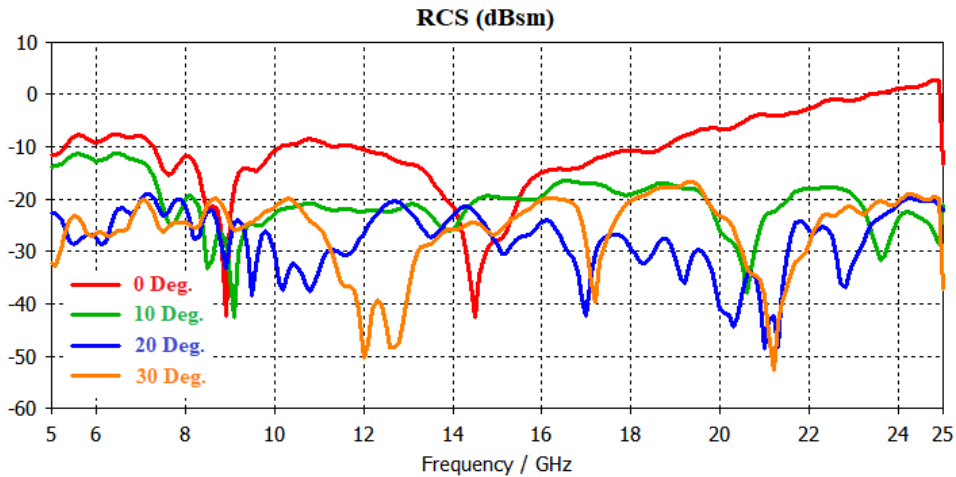**Figure 22.** RCS of the antenna with PCM under oblique incidence (TE mode).

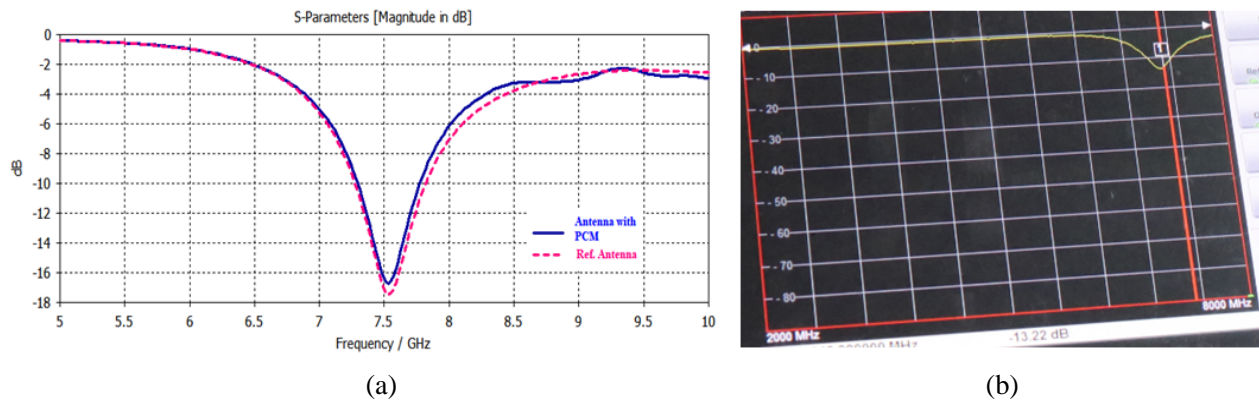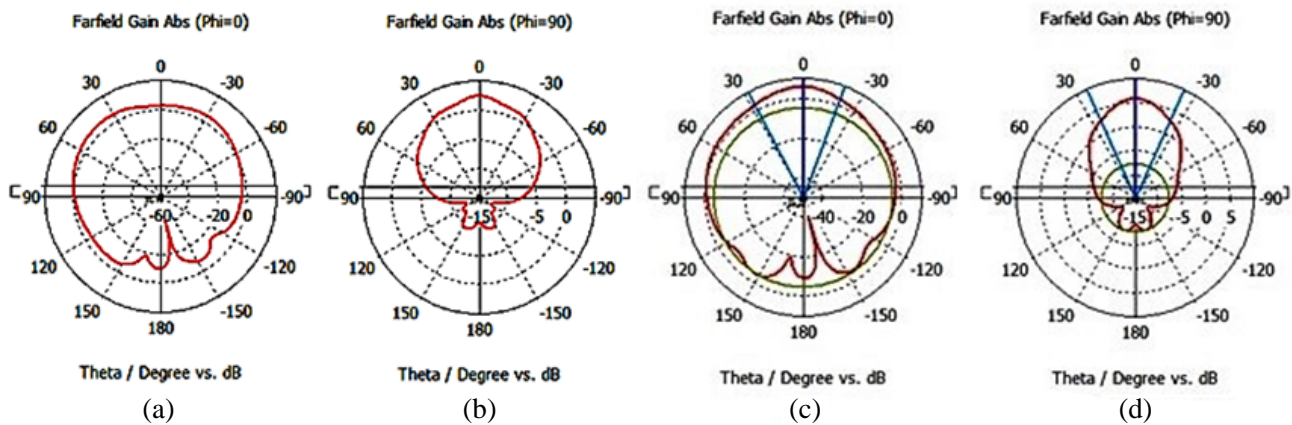**Figure 23.** RCS of the antenna with PCM under oblique incidence (TM mode).

(a)   (b)

Figure 24. (a) Simulated reflection coefficients of the Ref. Antenna (dashed) and the antenna with PCM (solid). (b) Experimentally measured reflection coefficient of the antenna with PCM.

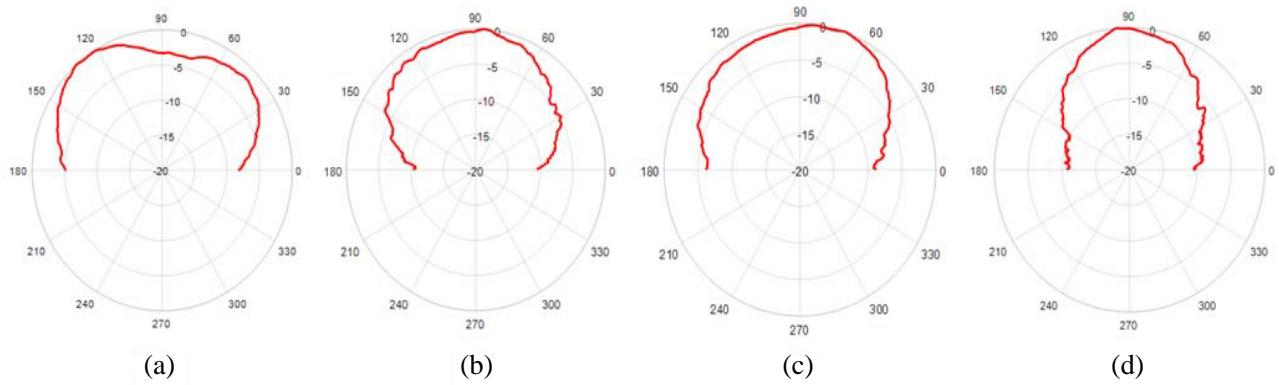(a)   (b)   (c)   (d)

Figure 25. Simulated far-field gain patterns of the Reference Antenna (a) $\phi = 0$ deg plane, (b) $\phi = 90$ deg plane, far-field gain patterns of the antenna with PCM, (c) $\phi = 0$ deg plane, (d) $\phi = 90$ deg plane.

of 7.5483 GHz. The experimentally measured reflection coefficient of the antenna with PCM is around -13.5 dB at the resonant frequency of 7.31 GHz. There is a good agreement between the simulated and experimentally measured results. Fig. 25 shows the simulated Gain patterns in the $\phi = 0$ deg plane and the $\phi = 90$ deg plane. For the reference antenna, the gain value is 2.385 dB in the boresight direction of the E-plane, and the peak gain value is 5.65 dB. The value of gain in the H-plane is 2.36 dB. For the antenna with PCM, the main lobe is directed at 0 deg in the E-plane and H-plane. The peak gain value is 5.81 dB in the $\phi = 0$ deg plane and $\phi = 90$ deg plane. So, as compared with the Reference antenna the radiation pattern of the antenna with PCM improves since it is directed at 0 deg in both the planes. The gain enhancement in the H-plane results from the slight mutual coupling of the metasurface elements and patch.

Figure 26 shows the experimental setup to measure the radiation patterns in the anechoic chamber. Absorber structures are used in the vicinity of the antennas to minimize unwanted reflections. Fig. 27 shows the experimentally measured radiation patterns of the conventional antenna in the $\phi = 0$ deg plane and $\phi = 90$ deg plane. The Friis-Transmission method is used to calculate the gain of the antennas. The measured gain value of the reference antenna is 2.87 dB in the boresight direction of the E-plane and 3.78 dB in the H-plane. The measured gain values of the antenna with PCM are 5.97 dB in the E-plane and 5.79 dB in the H-plane. The experimentally measured values are almost the same as those obtained by the simulation. Slight differences may be observed due to fabrication tolerances and line

<div align="center">(a)   (b)</div>
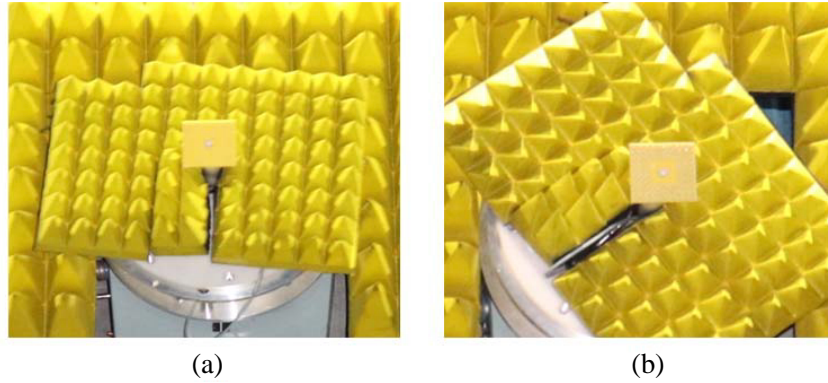
Figure 26. Experimental set-up for radiation pattern measurements in the anechoic chamber.

<div align="center">(a)   (b)   (c)   (d)</div>

Figure 27. Experimentally measured far-field radiation patterns of the reference antenna, (a) $\phi = 0\,\deg$ plane, (b) $\phi = 90\,\deg$ plane, experimentally measured far-field radiation patterns of the patch antenna with metasurface in (c) $\phi = 0\,\deg$ plane, (d) $\phi = 90\,\deg$ plane.

<div align="center">(a)   (b)</div>
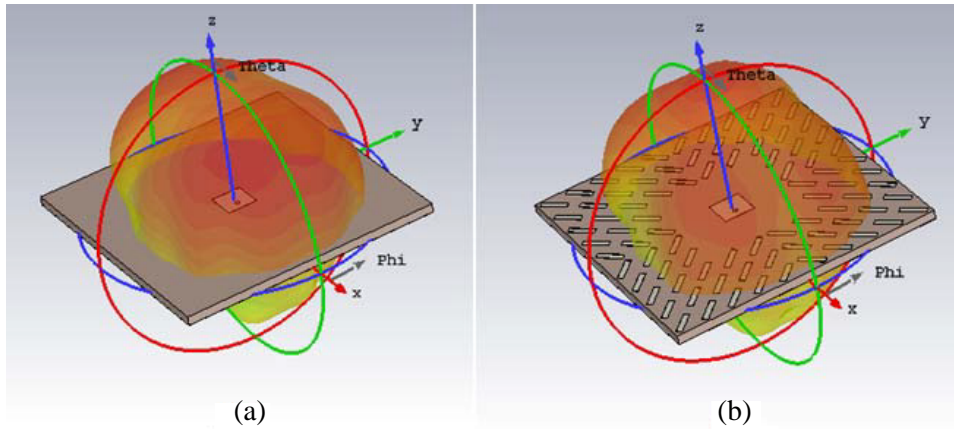
Figure 28. 3D gain patterns of (a) Reference Antenna, (b) antenna with metasurface.

losses. In the experimental polar patterns, the main lobe is directed at 90 deg due to the post-processing of the measurement data in the software. The experimental polar patterns are plotted from $-90\,\deg$ to $+90\,\deg$ since the positioner could not be rotated beyond 90 deg due to the supporting structure. Fig. 28 shows the 3D gain patterns of the reference antenna and the antenna with PCM at their resonant

frequencies. After analyzing the RCS values and the radiation patterns, it is observed that the proposed antenna shows excellent RCS reduction along with an improvement in the antenna radiation pattern.

The -10 dB impedance bandwidth of the antenna with PCM is from 7.3 GHz to 7.78 GHz (6.37%). So, in-band RCS reduction can also be obtained in addition to out-of-band RCS reduction.

Figure 29 shows the bistatic scattering at 9.1037 GHz frequency. The RCS values of the metal sheet, the reference patch, and the antenna with PCM are -5 dBsm, -5.1 dBsm, and -17.6 dBsm respectively in the phi $= 0$ deg plane. It shows RCS reduction of 12.6 dBsm and 12.5 dBsm as compared with the metal sheet and the reference patch. Fig. 30 shows the bistatic scattering RCS at 13.655 GHz frequency. The RCS values of the metal sheet, the reference patch, and the antenna with PCM are -1.89 dBsm, -3.42 dBsm, and -17.84 dBsm respectively in the phi $= 0$ deg plane. It shows RCS reduction of 15.95 dBsm and 14.42 dBsm as compared with the metal sheet and the reference patch respectively at this frequency. Significant RCS reduction is observed for a wide angular range. Bistatic RCS reduction can also be observed at the other resonance frequencies of PCM.

Figure 31 shows the 3D scattering comparison of the metal sheet, reference patch antenna, and the antenna with PCM at the frequency of 9.1037 GHz. In the cases of metal sheet and reference patch antenna, the reflected beam maxima are directed at 0 deg. For the antenna with PCM, the reflected beam is scattered in various directions, and the reflection is minimized in the boresight direction. So, RCS reduction mechanism can also be explained with the help of 3D scattering patterns.
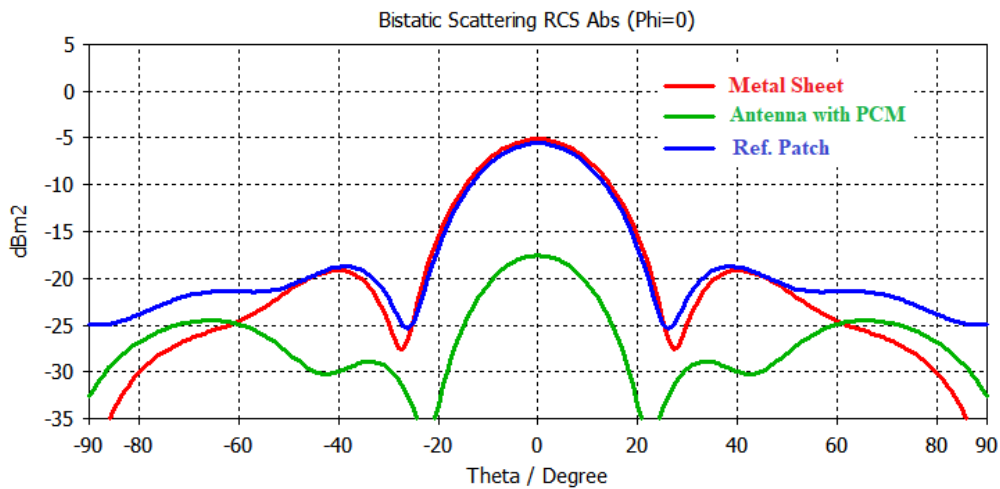

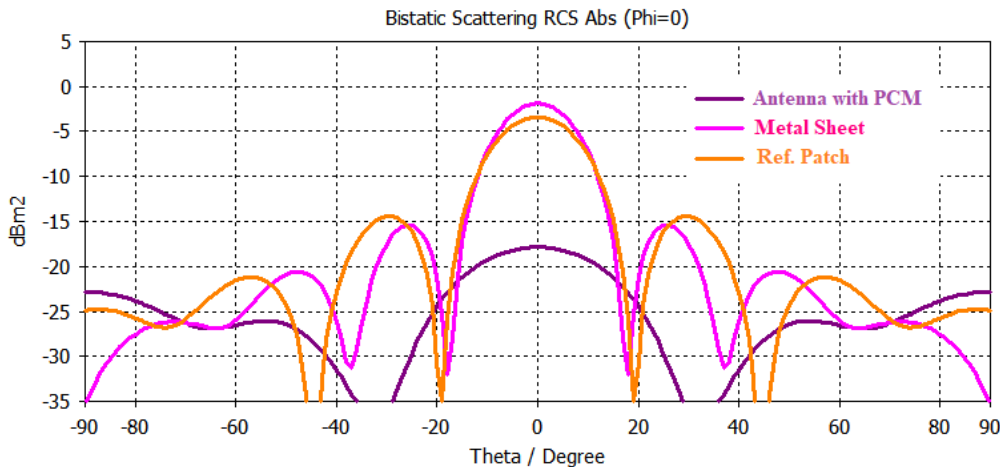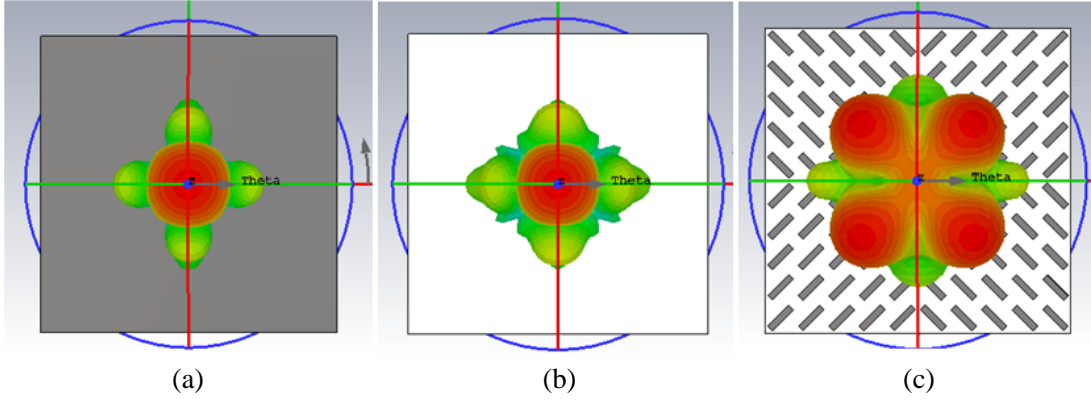**Figure 29.** Bistatic scattering at 9.1037 GHz.

Figure 30. Bistatic scattering at 13.655 GHz.

(a)   (b)   (c)

Figure 31. 3D scattering at the frequency of 9.1037 GHz, (a) metal sheet, (b) Reference Patch Antenna, (c) antenna with PCM.

Table 1. Comparison of the proposed design with similar work.

Ref., Year of Publication	Methodology Used	Features	Percentage Bandwidth	Design Complexity
[12], 2021	Polarization Converter Metasurface	Narrow BW, No discussion of Angular Stability	15.5 GHz–16.5 GHz (For linear to linear polarization conversion)	Not used for RCS reduction of patch antennas
[13], 2019	Jerusalem Cross based on Split Ring Resonator	Narrow Bandwidth	absorption peaks observed at 8.6, 10.2, 11.95 GHz	Not integrated with microstrip antenna
[9], 2018	Circular Ring with Parasitic Cross-AMC	Narrow Bandwidth	8.2–10.25 GHz (22.22%)	Not used for RCS reduction of antennas
[18], 2019	Optimized Coding Metasurface (AMC)	Narrow Bandwidth, No RCS reduction in the X-Band	12.2–19.8 GHz (48%) (> 7 dB RCS reduction BW)	Co-planar integration of the metasurface with the patch antenna
[8], 2017	Pixelated Checkerboard Metasurface	Comparatively narrow bandwidth	3.8–10.7 GHz (95.17%) (Overall)	Not used for RCS reduction of a patch antenna
[7], 2016	Polarization Converter Metasurface	No significant RCS reduction for a wide band	4.1–12 GHz (98.13%) (Overall)	Co-planar integration of the metasurface
[15], 2016	Polarization Rotator	Narrow Bandwidth for RCS reduction	5.50–8.94 GHz (47.75%) and 13.30–15.50 GHz (16.78%)	Simple and feasible design, Not used for RCS reduction of a patch antenna
Proposed Design	Polarization Converters	Wideband RCS reduction, In-band as well as Out-of-band RCS reduction, Good RCS reduction at oblique incidence	7.25 GHz–24.83 GHz (110%) (Overall), 10 dB RCS reduction BW 8.33 GHz–9.16 GHz (9.49%) and from 12.81 GHz–18.85 GHz (38.16%) as compared with the Ref. Patch	Co-planar integration of the metasurface with the patch antenna

From the simulated and experimental results, it can be inferred that for the patch antenna with PCM, no degradation of radiation pattern and gain is observed. Excellent Radar Cross Section reduction is obtained for the Transverse Electric as well as the TM mode. Significant RCS reduction can also be observed in the cases of oblique incidences. With this design, monostatic as well as bistatic RCS reduction can be obtained.

5. COMPARISON WITH PUBLISHED LITERATURE

Table 1 shows the advantages of the proposed design over the present state-of-the-art. The comparison is done in terms of percentage bandwidth of RCS reduction, radiation pattern characteristics, methodology used, and design complexity. It is observed from the comparison that most of the designs suffered from narrow bandwidth. Recently developed metasurfaces are not used to reduce the RCS of the patch antenna. The proposed design offers a wide RCS reduction bandwidth with an enhancement in radiation pattern characteristics as compared with the other designs.

6. CONCLUSION

A novel patch antenna is presented with a wideband cross polarization converter metasurface for radar cross section reduction. The proposed patch antenna shows the overall RCS reduction bandwidth of 7.25 GHz–24.83 GHz (110%) as compared with the metal sheet and the reference patch antenna. 10 dB RCS reduction is obtained from 8.33 GHz–9.16 GHz (9.49%) and from 12.81 GHz–18.85 GHz (38.16%) as compared with the reference patch antenna. Both in-band and out-of-band RCS reduction can be achieved for TE and TM polarizations. The wide bandwidth of RCS reduction is realized through multiple resonances of the polarization converter metasurface. RCS reduction can also be obtained for oblique incidences with shifts in resonant frequencies of the PCM structure. The radiation properties of the antenna are improved after metasurface loading. The wide RCS reduction bandwidth and improvement in the radiation pattern of the antenna make it a suitable candidate for combat platforms. It also proves the superior performance of the PCM over the other types of metasurface.

REFERENCES

1. Zheng, Y.-J., J. Gao, X.-Y. Cao, S.-J. Li, and W. Q. Li, "Wideband RCS reduction and gain enhancement microstrip antenna using chessboard configuration superstrate," *Microwave and Optical Technology Letters*, Vol. 57, No. 7, 1738–1741, 2015.

2. Yu, H., X. Cao, J. Gao, H. Yang, L. Jidi, J. Han, and T. Li, "Design of a wideband and reconfigurable polarization converter using a manipulable metasurface," *Opt. Mater. Express*, Vol. 8, 3373–3381, 2018.

3. Samadi, F. and A. Sebak, "Dielectric based triangle-type AMC structure for RCS reduction at mmWave frequencies," *IEEE International Symposium on Antennas and Propagation and North American Radio Science Meeting*, 1193–1194, 2020.

4. Liu, X., J. Gao, L. Xu, X. Cao, Y. Zhao, and S. Li, "A coding diffuse metasurface for RCS reduction," *IEEE Antennas and Wireless Propagation Letters*, Vol. 16, 724–727, 2017.

5. Kamal, B., J. Chen, Y. Ying, J. Ren, S. Ullah, and W. U. R. Khan, "High efficiency and ultra-wideband polarization converter based on an L-shaped metasurface," *Opt. Mater. Express*, Vol. 11, 1343–1352, 2021.

6. Kumar, P. V. and B. Ghosh, "Characteristic mode analysis of linear to circular polarization conversion metasurface," *Electromagnetics*, Vol. 40, No. 8, 605–612, 2020.

7. Liu, Y., Y. Hao, K. Li, and S. Gong, "Radar cross section reduction of a microstrip antenna based on polarization conversion metamaterial," *IEEE Antennas and Wireless Propagation Letters*, Vol. 15, 80–83, 2016.

8. Haji-Ahmadi, M. J., V. Nayyeri, M. Soleimani, et al., "Pixelated checkerboard metasurface for ultra-wideband radar cross section reduction," *Scientific Reports*, Vol. 7, 11437, 2017.

9. Zhang, X. L., M. Niu, L. H. Su, and K. P. Song, "Radar cross section reduction based on metasurface," *ChinaCom 2017: Communications and Networking*, B. Li, L. Shu, D. Zeng (eds.), *Lecture Notes of the Institute for Computer Sciences, Social Informatics and Telecommunications Engineering*, 236, Springer, Cham, 2018.

10. Ra'di, Y., C. R. Simovski, and S. A. Tretyakov, "Thin perfect absorbers for electromagnetic waves: Theory, design and realizations," *Phys. Rev. Appl.*, Vol. 3, No. 3, 037001, 2015.

11. Chen, H.-Y., P.-H. Zhou, L. Chen, and L.-J. Deng, "Study on the properties of surface waves in coated RAM layers and monostatic RCS performances of the coated slab," *Progress In Electromagnetics Research M*, Vol. 11, 123–135, 2010.

12. Pouyanfar, N., J. Nourinia, and C. Ghobadi, "Multiband and multifunctional polarization converter using an asymmetric metasurface," *Scientific Reports*, Vol. 11, 9306, 2021.

13. Jafari, F. S., M. Naderi, A. Hatami, and F. B. Zarrabi, "Microwave Jerusalem Cross absorber by metamaterial split ring resonator load to obtain polarization independence with triple band application," *AEU — International Journal of Electronics and Communications*, Vol. 101, 138–144, 2019.

14. Wang, S., M. Chen, J. Wang, Z. Zhang, Z. Li, and Y. Li, "Radar cross section reduction of a microstrip antenna with CSRRs loaded on the ground," *11th International Symposium on Antennas, Propagation and EM Theory (ISAPE)*, 670–673, Guilin, China, 2016.

15. Yang, D., H. Lin, and X. Huang, "Dual broadband metamaterial polarization converter in microwave regime," *Progress In Electromagnetics Research Letters*, Vol. 61, 71–76, 2016.

16. Shokati, E. and N. Granpateh, "High operative polarization converter using metasurface consisted of dual reciprocal L-shaped graphene array," *Journal of Nanophotonics*, Vol. 14, No. 1, 016015, 2020.

17. Qi, Y., B. Zhang, C. Liu, and X. Deng, "Ultra-broadband polarization conversion meta-surface and its application in polarization converter and RCS reduction," *IEEE Access*, Vol. 8, 116675–116684, 2020.

18. Li, J., K. T. Ali, X. Meng, J. Chen, G. Peng, and A. Zhang, "Wideband radar cross-section reduction of microstrip patch antenna using coding metasurface," *IET Microwaves, Antennas and Propagation*, Vol. 13, No. 10, 1719–1725, 2019.

19. Huang, L. and H. Chen, "Multi-band and polarization insensitive metamaterial absorber," *Progress In Electromagnetics Research*, Vol. 113, 103–110, 2011.

20. Yuan, H., H. Li, X. Fang, Y. Wang, and Q. Cao, "Active frequency selective surface absorber with point-to-point biasing control system," *IEEE Antennas and Wireless Propagation Letters*, 2021.

21. Balanis, C. A., *Antenna Theory: Analysis and Design*, Wiley, New York, USA, 2005.